ENGINEERING

A motoneuron discharge–driven interface realizing simultaneous and proportional control of prosthetics in end-users

Chen Chen[1,2]*†, Ruye Guo[1]†, Dongxuan Li[1]†, Shang Shi[1], Weichao Guo[2,3], Jianjun Meng[1,2], Guoying Gu[1,2]*, Xiangyang Zhu[1,2,3]*

Accurate decoding of movement intent from muscle signals is essential for dexterous prosthetic control. While motoneuron discharge decomposition provides a promising approach, most studies are confined to proof-of-concept demonstrations due to the lack of robust, dexterous control strategies, and the complexity of systems involved. Here, we present a motoneuron discharge–driven interface that integrates wireless recording of high-density surface electromyography, real-time motoneuron spike train decomposition, continuous multi-degree-of-freedom (DoF) motion decoding in a prosthetic system, enabling simultaneous and proportional myoelectric control in real-world settings. We validated this system with six trans-radial amputees across a series of functional multi-DoF tasks. The proposed interface achieved accurate and robust control of three-DoF wrist and hand movements, outperforming conventional myoelectric methods in task efficiency. Furthermore, the interface requires only single-DoF calibration data, minimizing user training burden. This study represents the practical demonstration of motoneuron-driven interfacing in end-user applications, highlighting its translational potential for clinical adoption.

INTRODUCTION

Dexterous and natural control of upper-limb prosthetic devices hinges on accurately decoding human motor intentions and converting them into actionable commands (*1*). Myoelectric interfaces, which rely on surface electromyography (sEMG) signals, are the most widely used due to their noninvasiveness and ability to capture muscle activation patterns (*2*, *3*). Early myoelectric interfaces relied on threshold-based methods to distinguish muscle activity, enabling simple control of a few prosthetic motions (*4*). Adopting machine learning models enables prediction of motor intentions based on time or frequency-domain features extracted from sEMG signals (*5*) and has demonstrated strong performance in hand gesture recognition and force estimation (*6*–*8*). Myoelectric interfaces have advanced rapidly and been commercially implemented in prosthetic control in recent years, yet still struggle to achieve simultaneous and proportional control (SPC) (*9*), where concurrent and continuous decoding of multiple degrees of freedom (DoFs) movements is required to achieve natural and intuitive prosthetic control.

One major source of this performance gap is the inherent complexity of sEMG signals (*10*). sEMG data represent the combined electrical activities of numerous motor units, each innervated by motoneurons originating in the spinal cord (*11*). When these signals are summed at the skin's surface, they offer an indirect and nonstationary glimpse into the precise neural commands that drive muscle contraction. The statistical features extracted from sEMG signals are often insufficient to capture the complexity and dynamic nature of motor control (*12*). For example, while time-domain and frequency-domain features can effectively classify discrete gestures, they lack the resolution to enable fine motor adjustments or SPC over multiple DoFs (*13*, *14*). In addition, a large sample size of training data is typically required to achieve competitive results (*15*, *16*).

A promising alternative is to decompose the sEMG signals into motoneuron discharges (*17*), which provides a direct representation of neural drive. Motoneurons in the spinal cord form the final common pathway for sending neural commands to the muscles. When these neurons discharge, they trigger activation in respective motor units, giving rise to the muscle activity that sEMG sensors detect (*18*). By extracting individual motoneuron discharge patterns rather than analyzing their summed electrical signals, a far more direct representation of the neural drive responsible for muscle contractions can be obtained, thereby improving the functionality and intuitiveness of prosthetic devices (*19*–*21*). Advances in sEMG decomposition techniques have made it feasible to extract individual motoneuron discharge trains (MNDTs) from surface recordings (*22*–*25*). Such an approach holds the potential to surpass conventional feature-based strategies, as it inherently targets the source of muscle activity, the spinal neural command, rather than its aggregated manifestation on the skin. Several studies have highlighted the superiority of motoneuron discharges over traditional sEMG features for gesture recognition and continuous movement estimation (*26*–*30*). For instance, decoding these discharges has facilitated more accurate predictions of finger forces and joint torques (*31*–*34*), which are crucial for prosthetic control systems that require real-time adaptation to dynamic tasks and user intentions.

In the past decade, motoneuron discharges have been explicitly applied in myoelectric control, and they are proposed as a promising solution for intuitive neural interfacing, providing a strong foundation for motoneuron-based prosthetic control (*2*, *17*, *25*, *29*). However, limited by the challenges of modeling multi-DoF movements and high computational resource requirements (*2*, *35*), previous

[1]State Key Laboratory of Mechanical System and Vibration, School of Mechanical Engineering, Shanghai Jiao Tong University, Shanghai, P. R. China. [2]Shanghai Key Laboratory of Intelligent Robotics, Shanghai Jiao Tong University, Shanghai, P. R. China. [3]Meta Robotics Institute, Shanghai Jiao Tong University, Shanghai, P. R. China.
*Corresponding author. Email: cedric_chen@sjtu.edu.cn (C.C.); guguoying@sjtu.edu.cn (G.G.); mexyzhu@sjtu.edu.cn (X.Z.)
†These authors contributed equally to this work.

studies mainly focused on proof-of-concept demonstrations in myoelectric control (*17*, *29*), where only theoretical investigations or tightly controlled experiments were conducted (*36*, *37*). This gap arises primarily from the challenge of embedding recording, decoding, and control modules into a compact prosthetic system. In addition, decoding motoneuron signals from residual limb muscles poses further challenges, including maintaining signal quality under varying conditions and translating the decoded information into functional prosthetic control (*38*).

In light of these considerations, the present work aims to bridge the gap between laboratory research and practical prosthetic control by introducing a motoneuron discharge–driven interface that integrates wireless high-density sEMG acquisition, real-time MNDT decomposition, and movement intent decoding into a prosthetic system. On the basis of the actual conditions of amputee end-users, we have integrated and optimized the neural-discharge-driven motion decoding methods, socket fabrication, electrode placement strategies, and control algorithms. The real-world applicability of the proposed interface was validated in real-time prosthetic manipulation experiments with six trans-radial amputee participants. Results demonstrated that our approach offered a direct and efficient pathway to achieve SPC of up to three DoFs (two DoFs of wrist and one of grasping) and surpassed traditional myoelectric interfaces.

RESULTS

The structure of the motoneuron discharge–driven interface was illustrated in Fig. 1. In brief, high-density sEMG signals were recorded from the residual muscles using three electrode grids, totaling 96 channels. The sEMG signals were wirelessly transmitted to a host laptop and then decomposed into MNDTs. The identified MNDTs were mapped to activations of multi-DoF movements and translated into control commands for the prosthetics. The hardware system for the interface is detailed in the supplementary data (fig. S1). To evaluate the interfacing performance of the proposed system, we recruited six trans-radial amputee participants to perform functional tasks (Table 1). Before functional validation, we analyzed motoneuron activity in the residual limb muscles (Fig. 2) and calibrated the control interface in a virtual test (fig. S2). Then, two experiments

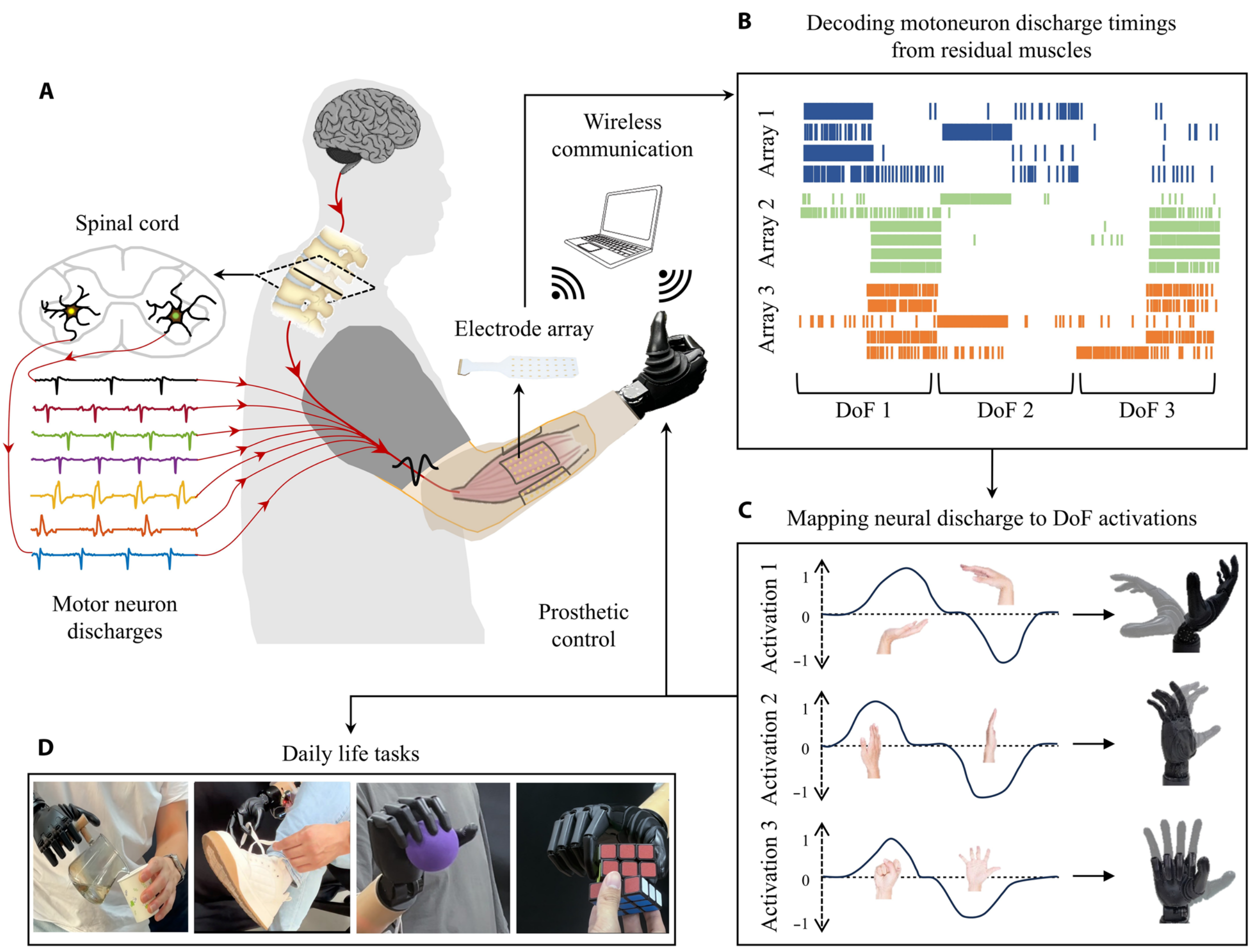

Fig. 1. Overview of the neural discharge-driven human-machine interface. (**A**) The prosthetic control system. High-density sEMG signals were recorded from residual muscles using three electrode grids and transmitted wirelessly to a laptop, where the motoneuron activities were decoded and translated to control commands for the prosthetics. (**B**) The interface provides access to the output from the spinal cord, MNDTs, as schematically represented by the colors from each grid. The discharge trains were decoded by blind source separation during a sequential 3-DoF movement. (**C**) The neural discharges were mapped to activations of three DoFs, and used to control the prosthetics to finish daily tasks as in (**D**).

Table 1. Participant characteristics. Dash entries indicate nonapplicable conditions.

Participant	Side	Gender	Age (amputation)	Residual limb	Own prosthesis	Frequency of use	Experienced myo-control
1	Bilateral, right tested	Male	39 (15)	Medium	2 DoF	Daily	High
2	Right	Male	45 (15)	Long	1 DoF	Seldom	Little
3	Left	Male	71 (18)	Medium	-	-	Little
4	Right	Male	34 (6)	Short	1 DoF	Seldom	Little
5	Right	Male	30 (2)	Medium	2 DoF	Seldom	High
6	Right	Female	42 (20)	Short	2 DoF	Daily	Medium

were performed to validate the control performance of the 2-DoF and 3-DoF functions: cylinder arrangement (Fig. 3) and foam ball placement (Fig. 4). Video recordings of all experiments are provided in the Supplementary Materials. Movie S1 presents the results of the virtual experiment before prosthetic use. Movies S2 to S4 illustrate task examples from both experiments, and movie S5 showcases participants performing daily tasks.

Decoding motoneuron activities from residual muscles

Before wearing the prosthetic socket, participants underwent electrode grid placement. All participants used three electrode grids for the prosthetic control experiments. The placement of the three electrode grids was determined by palpating the residual limb muscles to ensure optimal signal quality. After electrode grid placement, the participants donned the prosthetic socket (Fig. 2A). The connectors of the electrode grids were routed through openings in the socket and connected to a wireless adapter, enabling the wireless transmission of sEMG signals to the host laptop. The sEMG signals from each grid were individually decomposed using a motion-wise convolutional kernel compensation (mwCKC) algorithm (*39*) to obtain the discharge trains of motoneurons. Participants performed wrist and hand movements before and after wearing the prosthetic sockets, involving six actions in 3-DoF tasks or four actions in 2-DoF tasks (Fig. 2B). Despite the additional load of prosthetic gravity, the sEMG decomposition demonstrated stable MNDT decoding. The sEMG decomposition yielded 76 ± 29 MNDTs during 2-DoF tasks and 109 ± 43 MNDTs during 3-DoF tasks without prosthetics (Fig. 2D). When participants wore prosthetic sockets, the numbers of decoded MNDTs were 79 ± 20 and 99 ± 26 for 2-DoF and 3-DoF tasks, respectively, which showed no significant difference from those without prostheses. The accuracy of the decoded MNDTs was evaluated using an indirect metric, the pulse-to-noise ratio (PNR) (*40*). Across all tested conditions, the average PNR value was 30.4 ± 1.1 dB, indicating high reliability and accuracy in decoding motoneuron discharge activity (*40*). Further analysis of motoneuron firing rates indicates that the overall firing frequency remained within a similar range across control stages (fig. S3).

Following decoding, motoneurons were grouped on the basis of their firing correlations. The grouping involved calculating firing-rate profiles and paired correlation coefficients for the decoded motoneurons, followed by clustering with a consensus clustering algorithm (*41*). Without wearing the prosthetic socket, motoneurons decoded during 2-DoF tasks were grouped into 13 ± 4 clusters, while motoneurons from 3-DoF tasks were grouped into 17 ± 7 clusters (Fig. 2F). With the prosthetic socket, the clustering yielded a slightly increased average of 14 ± 4 clusters for 2-DoF tasks and 18 ± 3 clusters for 3-DoF tasks, reflecting the impact of additional muscle activation on the grouping process. The detailed decomposition and clustering results are shown in the Supplementary Materials (table S1). After clustering the MNDTs, the cumulative firing rates of each group were calculated and mapped to movement activations with a multiple linear regression (MLR) model. Before wearing the prosthetic socket, participants performed targeted achievement control (TAC) tasks in a virtual environment to validate the mapping process (*36*). The results of this virtual test, including sEMG decomposition and real-time interaction, are shown in the Supplementary Materials (table S2, fig. S2, and movie S1), which confirm the model's effectiveness in translating motoneuron activity into reliable action control.

Experiment 1: Cylinder arrangement

After the TAC test, participants performed a cylinder-arrangement task that required the SPC of two DoFs using the prosthetics (pronation/supination and hand closing/opening). Participants were instructed to complete a series of cylinder arrangements in this experiment. Two rows of pegboards were used, with one row holding five cylinders (Fig. 3A and movie S2). The participants were instructed to sequentially transfer each cylinder to the mirrored position on the opposite side of the other pegboard. The participant simultaneously activated two DoFs to transfer the cylinder, and the MNDT method accurately reflected the movement activations (Fig. 3, B and C). The predicted activation levels for each DoF were mapped to the prosthetic joint velocities, such that higher activation levels corresponded to faster movements. During cylinder transfers, the velocity and positional changes remained synchronized and smooth, validating the effectiveness of the proposed method in achieving SPC. In addition to velocity-based control, position-based control was explored, in which amputees were required to maintain contraction to control the prosthesis's reaching and holding at designated positions or angles (fig. S4). On the basis of feedback from participant 1, position-based control was more fatiguing during task execution. The following experiments were conducted using velocity-based control.

The performance of the proposed MNDT-driven prosthetic control strategy was compared with three conventional sEMG-based methods: nonnegative matrix factorization (NMF) (*42*), MLR (*1*), and pattern recognition (PR) (*26*). The efficiency of task completion was compared between different control methods and participants (Fig. 3E). The two-way analysis of variance (ANOVA) revealed

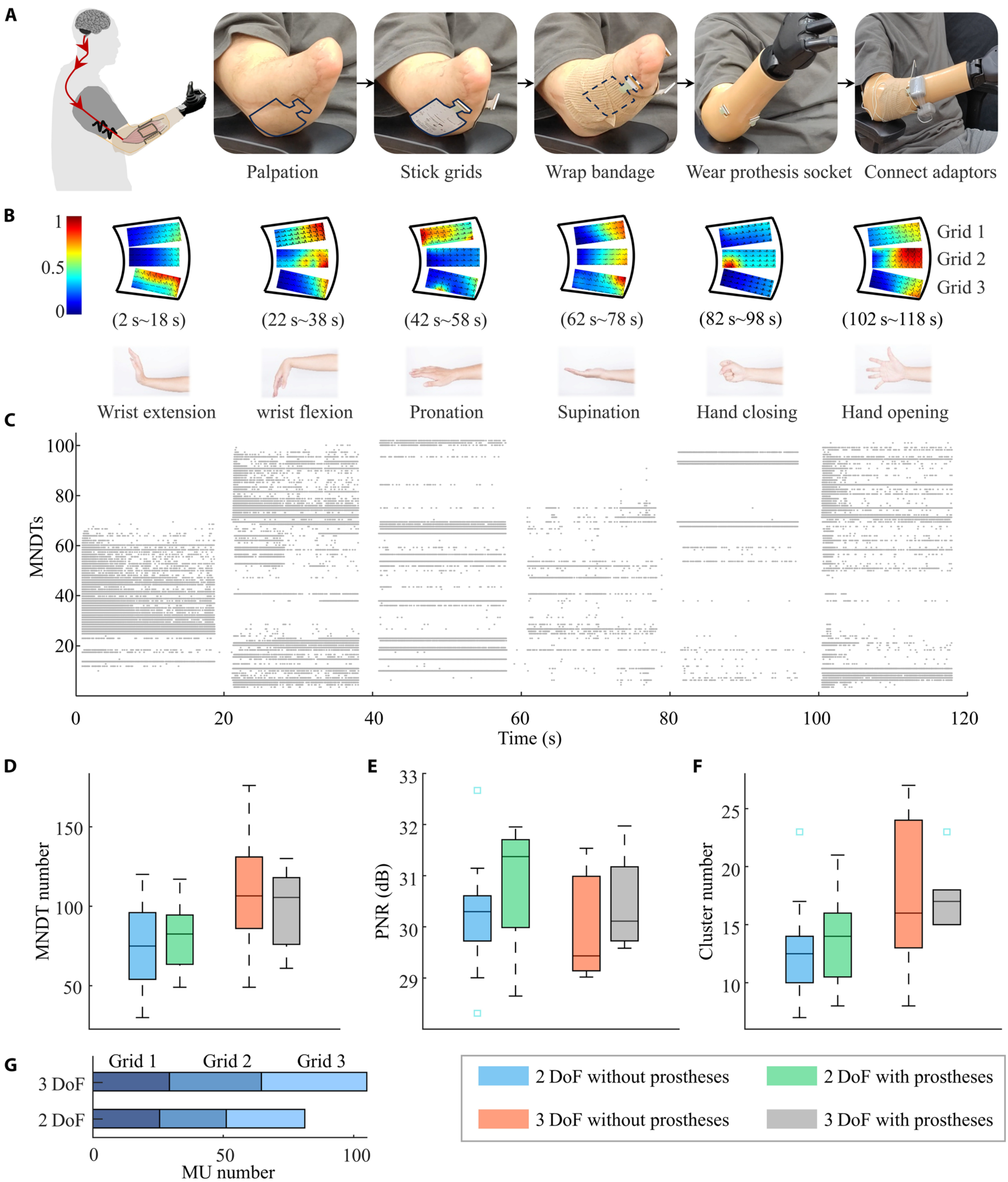

Fig. 2. Results of decoding motoneuron activities during the calibration process. (**A**) Fitting process for the amputee subject consisting of attaching the electrode grids, wearing the prosthetic socket, and connecting the sEMG signal acquisition device. (**B**) Average motor unit action potential (MUAP) waveforms and root mean square (RMS) activation maps of sEMG signals for each movement. The average MUAP waveform for each movement is obtained by summing and normalizing all MUAPs decomposed during that movement. The RMS activation map is generated by computing the RMS value of the sEMG signals at each electrode channel over the duration of the movement. The electrode positions reflect the actual spatial distribution of the electrodes. The execution sequence of movements includes wrist extension, wrist flexion, pronation, supination, hand closing, and hand opening. (**C**) Example MNDTs decomposed from a calibration phase. Scatters in each line indicate the discharge timings from a motoneuron. (**D** to **F**) The decomposition results during the 2/3-DoF movements and with/without prostheses, including the number of decomposed MNDTs, PNR, and the number of clusters. (**G**) The number of MNDTs decoded from each grid.

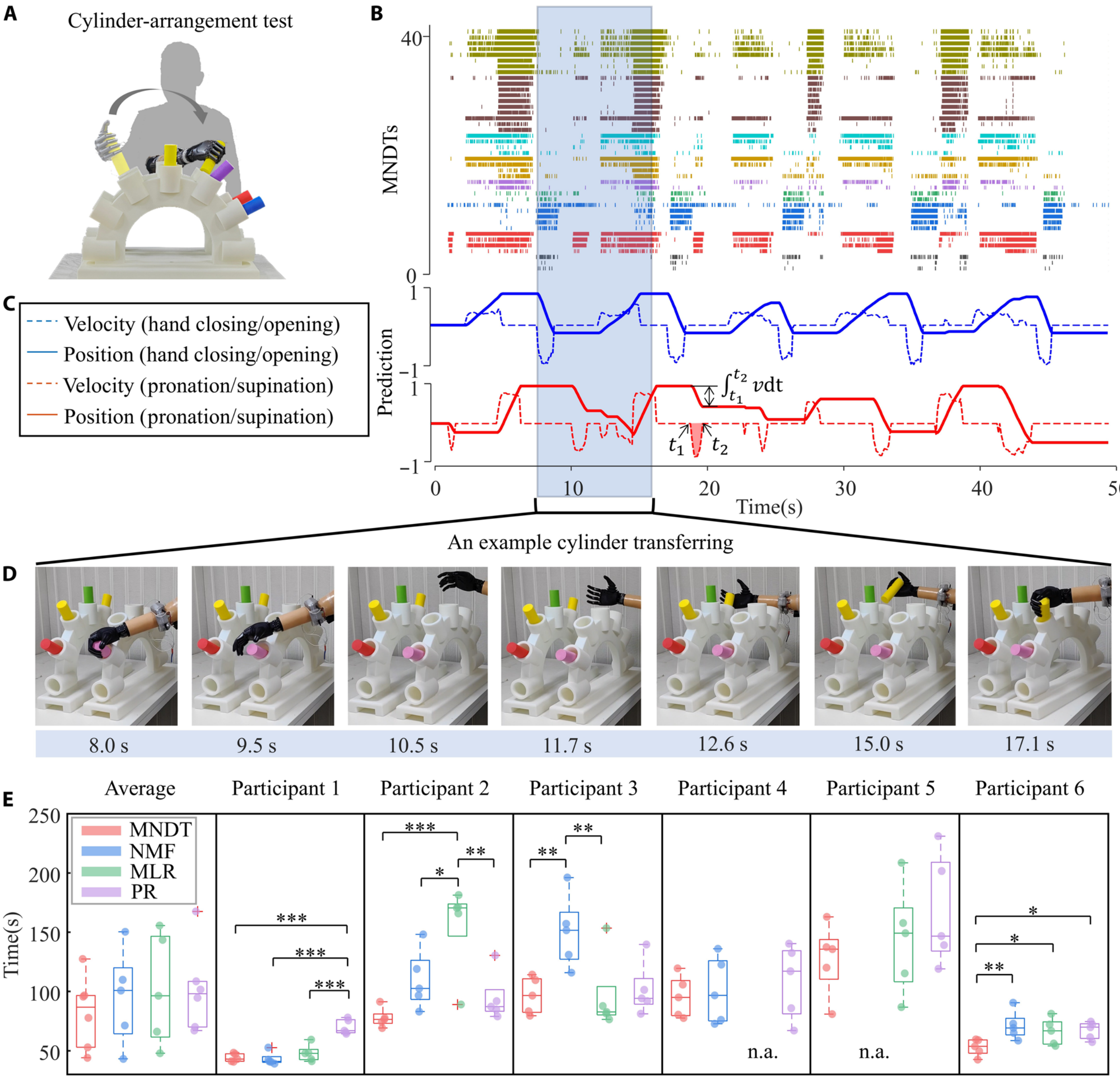

Fig. 3. Results from experiment 1: Cylinder arrangement. (**A**) Illustration of cylinder arrangement. In each trial, participants were required to transfer five cylinders from distant jacks to the opposite side of the close ones. (**B**) Example MNDTs decomposed in real time during a trial. The motoneurons are clustered into nine groups, distinct in different colors. (**C**) The velocity and position of the two DoFs of the prosthetic limb are represented in blue and red, corresponding to DoF1: hand closing (+)/hand opening (−) and DoF2: wrist pronation (+)/wrist supination (−), respectively. The dashed lines and solid lines represent the velocity and position of a certain DoF, respectively. (**D**) Chronophotography showing a participant performing the cylinder-arrangement test using the MNDT-based model with velocity control strategy. The time axis at the bottom corresponds to the time in (B) and (C). The data are from participant 1. (**E**) The time required to transfer five cylinders is displayed. The performances of the MNDT-based method and the other three sEMG-based methods (NMF, MLR, and PR) are shown separately for each participant (one panel each). Symbols (∗, ∗∗, and ∗∗∗) indicate the significant difference between groups with a level of ($0.01 < P < 0.05$), ($0.001 \le P \le 0.01$), and ($P < 0.001$), respectively. n.a. stands for not applicable.

significant main effects of method ($P < 0.01$), and participant ($P < 0.001$), and a significant interaction effect ($P < 0.01$). When analyzing performance within each participant, completion times for different control strategies varied greatly across participants. For participant 1, the task completion times using the MNDT, NMF, and MLR methods were significantly better than those of the PR method, demonstrating the superior efficiency of the SPC. For participant 2, the MNDT method outperformed the other two SPC strategies, and participant 2 also adapted well to using the PR method for control. For participant 3, the NMF method was significantly worse than the other three methods, while no significant differences were observed between the remaining methods. For participants 4 and 5, two control strategies failed to complete the tasks. Among the remaining three control strategies, the MNDT method required less time to complete the task than the others. For participant 6, the completion time of the MNDT method was significantly less than that of the other control methods. Overall, despite the significant individual differences, the MNDT method demonstrated high efficiency and stability in the two-DoF tasks.

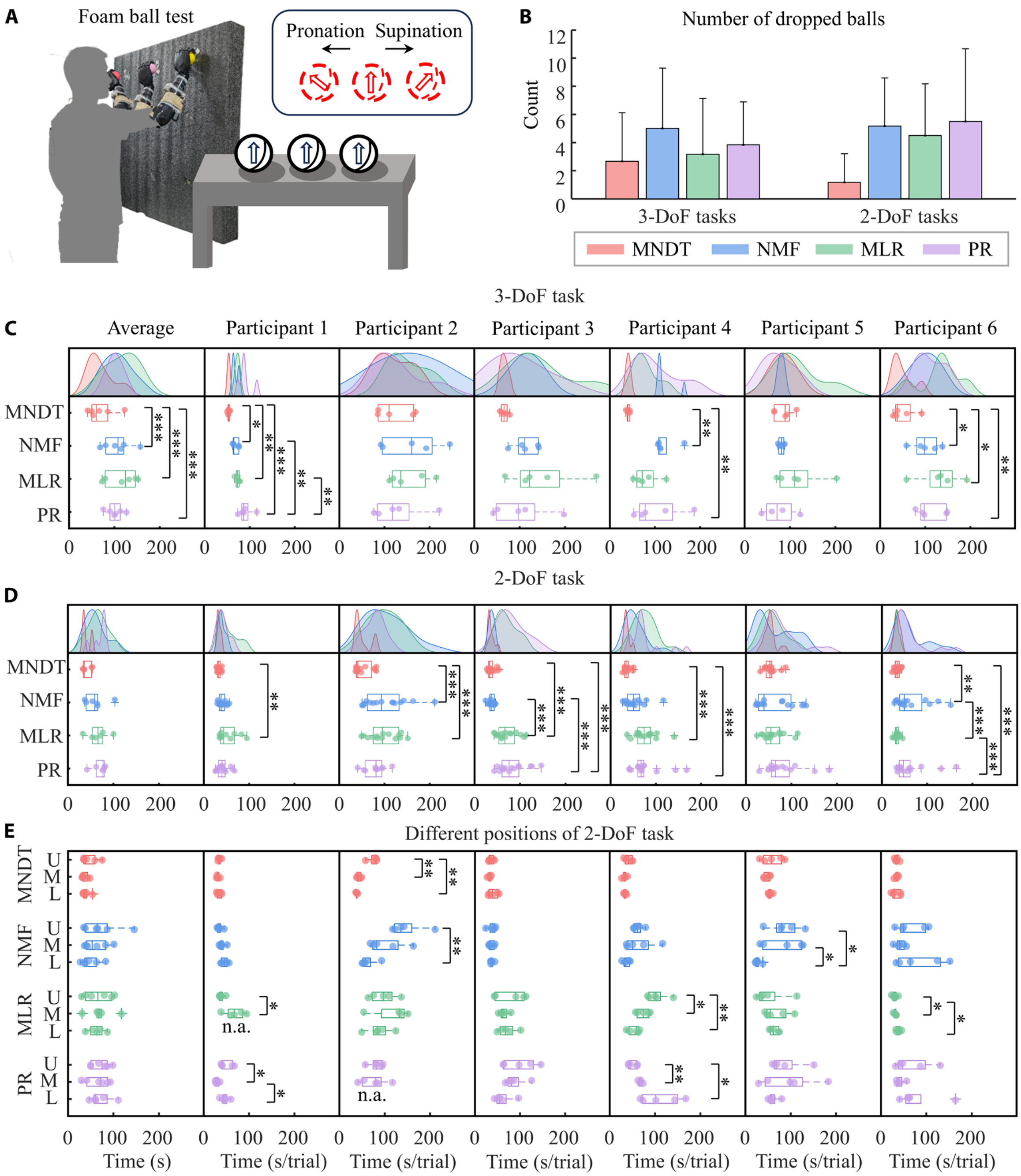

Fig. 4. Results from experiment 2: Foam ball placement. (**A**) Illustration of the 3-DoF foam ball task. In each trial, participants were required to pick up three balls one by one from the table and transfer them to the target position. (**B**) The total number of ball drops for each model in both 2-DoF and 3-DoF tasks, with data representing the average across participants. (**C**) The completion time of each trial in the 3-DoF task. The upper part shows a half-violin plot, while the lower part shows a box plot. Performances of the MNDT-based method and the other three sEMG-based methods (NMF, MLR, and PR) are shown separately for each participant. (**D**) The completion time of each trial in the 2-DoF task. In the 2-DoF tasks, additional tests were conducted at the upper (U), middle (M), and lower (L) arm positions. The completion times for each participant at the three arm positions were pooled together. (**E**) The completion time of tasks in three arm positions. Symbols (*, **, ***) indicate the significant difference between groups with a level of ($0.01 < P < 0.05$), ($0.001 \leq P \leq 0.01$), and ($P < 0.001$), respectively. n.a. stands for not applicable.

Experiment 2: Foam ball placement

Following the cylinder arrangement experiment, participants were instructed to finish a 3-DoF control task, where they transferred three foam balls from the table to the target area and aligned the arrow on each foam ball by performing wrist extension/flexion, pronation/supination, and hand closing/opening simultaneously (Fig. 4A). The control strategies were similar to those in the cylinder arrangement test but adapted to 3-DoF tasks. The control efficiency, as indicated by the completion time of the 3-DoF task, was compared between participants and control methods (Fig. 4C). The two-way ANOVA identified significant main effects of method ($P < 0.001$) and participant ($P < 0.001$), while the interaction was not significant ($P = 0.242$). Overall, the MNDT method demonstrated superior performance over the other three schemes ($P < 0.001$). For three participants, the MNDT method exhibited significantly less completion time. In addition, the MNDT method had the most concentrated distribution of task completion times across repetitive trials. In contrast, other methods exhibited greater instability, sometimes causing the ball to fall off (Fig. 4B). Among the four methods, the MNDT method resulted in the fewest instances of the ball falling off, indicating the most stable and reliable control performance. The examples of the 3-DoF control tasks in experiment 2, including MNDTs, prosthetic commands, and chronophotography, are shown in the Supplementary Materials (fig. S5 and movie S3). For participant 1, we further analyzed the stages during which SPC occurred and calculated the proportion of each movement combination among all SPC occurrences (fig. S6 and table S3). Two dominant 3-DoF simultaneous control patterns, hand opening with pronation/extension and hand opening with pronation/flexion, were identified most frequently when reaching targets on the left. While simultaneous control reduced task completion time compared to sequential control, participants tended to switch to sequential control for supination-involved motions due to their higher difficulty, demonstrating the system's adaptive flexibility in control mode switching.

The effect of arm position on prosthetic function was also tested (Fig. 4, D and E). Participants were instructed to place the balls onto the horizontally aligned target points on the foam board at three arm positions (upper, middle, and lower). Participants only performed 2-DoF control (wrist extension/flexion and hand closing/opening) without ball rotation to reduce the experimental burden. The data used to calibrate the model were recorded at the middle arm position. The task completion times for the 2-DoF task, which combines data from three positions, are presented in Fig. 4D. The two-way ANOVA revealed a significant interaction effect between participants and methods ($P < 0.001$), as well as significant main effects of method ($P < 0.001$) and participant ($P < 0.001$). Furthermore, to assess the effect of arm position on performance (Fig. 4E), separate two-way ANOVAs were conducted for each method, with participant and arm position as factors. For the MNDT and NMF methods, significant main effects of participant and arm position, as well as a significant interaction, were observed. For the MLR and PR methods, the main effect of participant and the interaction were significant, whereas the main effect of arm position was not significant. Because the interaction term was significant, follow-up analyses were performed within each participant to further examine the effect of arm position. In the 2-DoF tasks, the MNDT method remains the optimal choice, as no other method significantly outperformed it in completion time across all scenarios. When using the MNDT method, all participants, except participant 2, showed no significant differences in task completion times across the three positions. In contrast, other methods were influenced by position, with most participants taking longer to complete when switching positions. For certain methods, specific positions even caused the control strategies to fail (e.g., participant 1 with MLR and participant 2 with PR). The MNDT method generally resulted in lower overall completion times among all participants, indicating that it offers robust control across different arm positions. An example of the 2-DoF task is illustrated in the Supplementary Materials (fig. S7 and movie S4).

DISCUSSION

Upper-limb prosthetics represent a canonical challenge in human-robot interaction. To address this, our study introduces a motoneuron discharge–driven interface that successfully achieves SPC of prosthetics. The results demonstrated the superior performance of the motoneuron discharge–based control across both 2-DoF and 3-DoF tasks, highlighting the advantages of the MNDT-based method in efficiency, accuracy, and robustness, particularly for tasks that require the SPC of multiple DoFs. Following a simple calibration step involving single-DoF movements, users were able to simultaneously control multi-DoFs of the wrist and hand. The MNDT-based control strategy exhibited notable advantages in both 2-DoF and 3-DoF tasks, especially in the latter. Performance varied across participants in multi-DoF control experiments, with some participants completing the tasks using all control strategies but with significantly longer completion times for NMF or MLR methods. The failure of NMF in some participants likely stemmed from the functional and distributional limitations of residual limb muscles, which hindered the extraction of sufficient information about the coordination of antagonist muscles. Similarly, the MLR method struggled with stability and precision as the number of DoFs increased, making it difficult to extract reliable activation information for each DoF and, in some cases, failing to achieve functional control in 3-DoF tasks. These results underscore the robustness of the MNDT-based control strategy, which consistently achieved efficient task performance regardless of task complexity or participant variability. While this study focused on three DoFs (pronation/supination, wrist flexion/extension, and hand closing/opening), the proposed MNDT-based control strategy is extensible to other joints and movements. The system does not rely on task- or muscle-specific assumptions for motoneuron decoding or movement mapping, making it a general neural interface capable of accurately decoding efferent neural activity and movement intentions.

Prior work has made valuable advances in the neural interfacing of prosthetics, such as proof-of-concept demonstrations of MNDT's interactive performance in offline, virtual experiments (*36*) or mixed virtual/socket-attached demonstrations (*29*). Building on these efforts, the present study proposes an MNDT-driven interfacing framework that enables SPC of up to 3 DoFs. Furthermore, this study focuses on demonstrating the practicality of motoneuron-based control for prosthesis-wearing amputees. We integrated sEMG acquisition, MNDT decoding, and control methods into the prosthetic socket, thereby validating the feasibility and superiority of MNDT for prosthetic control from the end-user perspective. The methodological refinements in hardware include signal acquisition manner, socket ergonomic design, and electrode positioning. In addition, the training protocols, control strategies, and scaling factors had to be optimized to accommodate amputee users. These advancements collectively facilitate the clinical translation of motoneuron-driven interfacing into functional prosthetic applications. PR methods are frequently used in multi-DoF prosthetic control and have been demonstrated to be a straightforward and effective approach (*43*, *44*), as also confirmed by the findings of this study. However, because of the inherent characteristics of PR methods, they cannot activate multiple DoFs simultaneously as a human hand does, generally resulting in lower control efficiency than SPC strategies. In contrast, the proposed method enabled the SPC of three DoFs by interpreting neural discharge signals, allowing participants to perform operational tasks more naturally and dexterously. Results showed that the MNDT-based method achieved a higher SPC proportion compared to the other methods, demonstrating the substantial potential of MNDT in human-machine interaction applications such as prosthetics.

To develop an MNDT-based neural interface, two critical components are essential. The first one is sEMG decomposition, which enables noninvasive access to MNDTs from residual muscles. sEMG signals are complex mixtures of action potentials from thousands of motoneurons and are inherently nonstationary. This complexity is particularly pronounced in the forearm, where overlapping muscles produce mixed sEMG signals, making it challenging to extract DoF-specific information with traditional sEMG features. By decomposing MNDTs, we could isolate the neural source signals driving muscle activity, thereby providing more accurate neural drive information. Unlike conventional sEMG features, these MNDTs provide a microscopic view of neural drive, enabling a direct approach to decoding human movements. The key distinction of this work from prior research lies in its focus on real-world prosthetic use, where the muscle distributions and motion execution capabilities of amputees vary observably with their residual limb conditions and training history. Furthermore, the integration of electrode arrays within the prosthetic socket introduces unique challenges for sEMG decomposition due to electrode compression and gravitational effects. To overcome these limitations, we explored a task-segmented sEMG decomposition strategy that enhances decoding of MNDTs (*26*). Whereas existing studies involving amputees or patients with targeted muscle reinnervation typically identify fewer than 50 discriminable motoneurons (*38*), our approach demonstrates both high efficiency and stability in motoneuron decoding. This improvement highlights the proposed method's potential to capture detailed neural activity in practical applications.

After decoding the MNDTs, the next challenge was mapping these discharges to prosthetic control commands. Prior work established a direct one-to-one relationship between motoneuron groups and movements based on their discharge timing (*45*). However, for wrist and hand movements, where muscle activation overlaps across multiple DoFs, most motoneurons are activated across multiple movements, making it difficult to establish a direct mapping for more than three movements (*45*). To address this, we adopted a discharge correlation-based motoneuron grouping approach (*36*), which calculates motoneuron firing rates and correlations, followed by clustering using a consensus clustering algorithm. The cluster-based framework demonstrated considerable robustness against potential instabilities in the decomposition process. As validated by simulations of random motoneuron loss (fig. S8), the control system maintained high performance even with the loss of ~10% of motoneurons. As each cluster contains multiple motoneurons, the loss of a few MNDTs only causes a minor reduction in the cumulative spike train (CST) firing rate of that cluster, ensuring the stability in online control. For newly recruited motoneurons during task execution, we did not consider them due to the lack of mature solutions currently available. Nevertheless, some studies have attempted to address these issues (*46*), and these decoding approaches are not incompatible with our proposed neural-driven interfacing framework, further demonstrating its potential for further refinement and enhancement. Notably, the proposed motoneuron-driven control interface requires only minimal training. Before executing multi-DoF tasks, amputees were merely familiarized with the experimental protocol and the TAC test. Following prosthesis donning, model calibration was achieved solely through single-DoF motion sequences, with a total training duration of under 2 min. This exemplifies a key advantage of our neural interface: rapid calibration via ultra-brief data acquisition, which prominently reduces user training burden and enables immediate postdonning functionality.

The MNDT method consistently outperformed conventional controllers among all trans-radial participants in both experiments 1 and 2. Notably, participants who achieved high-level performance on one task with MNDT tended to show similarly strong performance on the other, indicating robustness and predictive consistency across tasks. Furthermore, the MNDT approach demonstrated superior stability across upper, middle, and lower arm positions compared to traditional methods, which exhibited measurable performance variations with positional changes. The stability and robustness are likely attributable to the motoneuron-level neural drive extraction, which is less affected by intersubject variability and residual limb conditions compared with classic approaches. By contrast, the performance of NMF-, regression-, and PR-based controllers varied substantially across participants and tasks, reflecting their lower generalizability. In addition, no clear association was found between prior myoelectric control experience and task performance. All participants were equally unfamiliar with the simultaneous hand-wrist control paradigm and received standardized familiarization training, minimizing the influence of prior experience in the present study. It should be noted that the order of the four methods in each experiment was random. The four control models appeared in different positions across participants, which reduce the risk of systematic bias (table S4).

A limitation of the proposed control interface is that the computational module has not yet been integrated into the prosthetic socket. Given current computational complexity and hardware capabilities, achieving onboard decomposition and analysis remains challenging. However, with ongoing advancements in hardware capabilities, full integration is not a fundamental barrier. In addition, specialized protocols for SPC evaluation were adopted in this study. Other standardized assessments, such as the clothespin relocation test and ACMC, would be implemented in the future and strengthen the practicability of the proposed interface.

In conclusion, this study demonstrated the feasibility and superiority of the proposed motoneuron discharge–driven interfacing framework in end-user applications. By integrating high-density sEMG recording, decomposition, mapping, and control modules, six amputees achieved in vivo real-time measurement of motoneuron discharges and SPC of up to three DoFs of an upper-limb prosthesis. The results provide a clear foundation for neural discharge-driven control to enhance prosthetic functionality and clinical translation for end-user applications. Furthermore, this interface serves as a platform technology with direct applicability beyond prosthetics, including exoskeletons, rehabilitation robotics, and human-virtual environment interactions.

MATERIALS AND METHODS

Participants

We recruited six participants with trans-radial amputations whose characteristics relevant to this study are reported in Table 1. The participants had no prior neuromuscular disorders. They were informed about the experimental procedure and signed informed consent forms before participation. The experimental protocols and informed consent forms were approved by the ethics committee of Shanghai Jiao Tong University (approval number E20240248I).

Experimental setup

sEMG recording

In the experiments, sEMG signals were recorded with three flexible electrode grids. The placement of the grids differed across individuals and corresponded to the activation of residual muscles. Before electrode placement, the participants were instructed to perform wrist and hand movements, and the activation areas were ensured by palpation. Each grid comprises 32 electrodes (8 × 4, 3 mm diameter, GR10MM0804, OT Bioelettronica, Italy) with a 10-mm interelectrode distance in both directions. The grids were pasted on the skin surface by a 1-mm-thick double-adhesive foam with holes corresponding to the electrode locations. The skin-electrode contact was facilitated by conductive paste. The electrode grid was connected to a Muovi probe, which collected sEMG signals from 32 channels and wirelessly transmitted them to a synchronization station (MuoviPro, OT Bioelettronica, Italy). The synchronization station was connected to a laptop, where the sEMG signals were decomposed and analyzed. The sEMG signals were sampled at 2000 Hz and A/D-converted with a 16-bit resolution.

Prosthetics

The prosthetic system used in the experiment is a multi-DoF anthropomorphic prosthetic hand/wrist (SJT-7) designed and fabricated by our team (*47*). The prosthesis has six active DoFs, including two thumb DoFs (abduction and adduction), one index finger DoF (flexion), one three-finger DoF (flexion), and two wrist DoFs. The wrist extension/flexion range is (−30° to 30°), and the wrist rotation range is (−45° to 45°). The prosthesis is equipped with Bluetooth signal reception capabilities. During the experiment, the laptop analyzes the sEMG signals, decodes the participant's motor intentions, and converts them into control commands for the prosthetics. These commands are transmitted to the prosthetic control module via Bluetooth. Before participants wore the prosthetics, a customized socket was fabricated for each using traditional prosthetic fitting techniques. A plaster negative of the residual limb was created, which was then used to form a plaster-positive mold from gypsum. We created a single-layer socket to facilitate the placement of electrode grids. After determining the positions for the electrode grids, we made openings in the thermoplastic socket at the plug. The participant first attached the electrode grids and wore the socket during the fitting process. Then, the grid plugs were passed through the openings and connected to the probe (Fig. 2A).

Experiment protocol

For upper-limb prostheses, grasping represents one of the most critical functions. While grasping in various postures, wrist DoFs adjustment proves essential for both stability and flexibility. Therefore, after considering prosthetic operation requirements and actual functional capabilities, we selected three DoFs as control targets: hand closing/opening, pronation/supination, and wrist extension/flexion. Before conducting the prosthetic control, participants underwent a model calibration experiment, performing a series of single-DoF tasks for each DoF involved (detailed in the "Motoneuron-based control strategy" section). Upon completion of the model calibration, participants proceeded to control performance tests in a virtual environment, where they controlled the movement of a cursor using multi-DoF motions to move it to specified locations (fig. S2 and movie S1).

Considering the operational performance of the prosthetic hand and the wrist-hand DoFs to be validated, we designed two specific functional tasks: cylinder arrangement and foam ball placement. These tasks mimicked natural movements and satisfied the testing requirements. Notably, several standardized assessments exist for evaluating prosthetic control, such as the ACMC (*48*), AM-ULA (*49*), and the clothespin relocation test (*1*). Although practical reasons prevented us from adopting these standard tests, the task paradigm we designed was inspired by them, and some task types and metrics share similarities. Participants used pronation/supination and hand closing/opening DoFs in the cylinder arrangement task. Each trial involved positioning five cylinders from a distant jack field into a close one sequentially, with the cylinders being transferred from the jack on the right/left side to the opposite one on the left/right side (e.g., from the right-most jack in the distant field to the left-most jack in the close field; Fig. 3A). Each participant was required to repeat the trial five times. After completing five trials, the control model was changed (e.g., NMF, MLR, and PR), and the same tasks were implemented. The completion time for each trial was recorded and analyzed. At the end of the experiment, the 20 tasks of online test data from four control models were saved for further analysis. The order of control models was randomized in each experiment (table S4).

In the foam ball placement experiment, we prioritized the 3-DoF task of wrist extension/flexion, pronation/supination, and hand opening/closing. In this experiment, participants faced a foam board with dimensions of 10 cm in thickness and 1 × 1 m^2 in area. Nine target points were marked on the foam board in a 3 × 3 grid arrangement, with each adjacent pair of targets, both horizontally and vertically, spaced 40 cm apart (Fig. 4A). The foam board was positioned against a wall and elevated such that its central target row aligned with the participants' elbow height. Three small balls were placed on the experimental table in front of the board, spatially corresponding to the horizontal target points on the foam board. Arrow markers were affixed to the small balls. The foam board was also marked with arrow markers at three positions (from left to right), indicating 45° counterclockwise rotation, no rotation, and 45° clockwise rotation relative to the small ball. In each trial, participants were asked to place three balls in the corresponding positions on the foam board, ensuring that the arrows on the balls aligned with the arrows on the foam board. The 3-DoF control tasks were completed at the top position of the foam board. Participants were required to complete five repetitive trials of the task for each model. The completion time for each trial was recorded and analyzed, and a total of 20 sets of online test data from the four models were saved.

Previous studies have shown that changes in arm position can negatively affect the performance of the control model (*1*). In this experiment, the effect of arm position was also taken into consideration. Participants performed 2-DoF control (wrist extension/flexion and hand closing/opening) to reduce the experimental burden. Participants were instructed to place the balls onto the horizontally aligned target points on the foam board at three arm positions (upper, middle, and lower). The data recorded at the middle arm position were used to calibrate the control model. The total time taken by the participants to place all three balls on the corresponding target points was recorded. Each participant completed five repetitions of the task at each arm position, resulting in 15 sets of online test data for each control model. The completion times for each set were recorded. A total of 60 sets of online test data from the four models were saved. The experimental order for each model and arm position was randomized.

Motoneuron-based control strategy

sEMG decomposition

sEMG decomposition is performed in two steps. During the model calibration phase, sEMG signals are decomposed offline using a blind source separation method to obtain separation vectors and other decomposition parameters. During the real-time prosthetic control phase, the sEMG signals are decomposed online using the preobtained decomposition parameters.

In the offline phase, a motion-wise decomposition method was used to decompose the sEMG signals (*39*). The sEMG signals from each motion were regarded as a segment and decomposed into MNDTs individually using the convolution kernel compensation (CKC) algorithm. A brief introduction to the decomposition algorithm is given. The sEMG signals are generally modeled as a multi-input-multi-output system

$$x_i(n) = \sum_{j=1}^{J} \sum_{l=0}^{L-1} h_{ij}(l)\theta_j(n-l) + w_i(n), i = 1, 2, \ldots, M \quad (1)$$

where x_i denotes the sEMG signal from ith channel, n is the sample point, θ_j is the discharge train of the jth motoneuron and h_{ij} is the corresponding pulse response, L is the sample length of the action potentials, w_i is the additive noise signal for the ith channel, and J and M are the numbers of active motoneurons and sEMG channels, respectively.

The mixing model, as denoted by Eq. 1, is similar to a Bayesian linear model. As the mathematical expectation of sEMG (x) and discharge trains (θ) are close to zero, the LMMSE estimations of the discharge train can be written as

$$\widehat{\theta} = C_{\theta x}^{T} C_{xx}^{-1} x \quad (2)$$

where $C_{\theta x} = \left[c_{\theta_1 x}, c_{\theta_2 x}, \ldots, c_{\theta_J x}\right]$ contains the cross-correlation vector between each discharge train and sEMG signals, and $C_{xx} = E\left(xx^T\right)$ is the covariance matrix of sEMG signals, and E denotes the mathematical expectation. The CKC algorithms used Eq. 2 to estimate the MNDTs, where the $c_{\theta_j \overline{x}}$ can be estimated iteratively using a natural gradient descent method

$$\widehat{c}_{\theta_j \overline{x}, k+1} = \widehat{c}_{\theta_j \overline{x}, k} + l \sum_{n} \frac{\partial f\left[\widehat{\theta}_j(n)\right]}{\partial \widehat{\theta}_j(n)} \overline{x}(n) \quad (3)$$

where $\widehat{\theta}_j$ is the jth discharge train estimated depending on Eq. 2 in each iteration, l is the learning rate, and $f(t)$ is the cost function. The $\frac{\partial f(t)}{\partial t}$ should be the concave even function (*50*), which was set as $\frac{\partial f(t)}{\partial t} = t^2$ in this study.

The single-DoF motions in the calibration dataset were decomposed offline using the mwCKC algorithm (*39*). This decomposition was implemented individually for each electrode grid. Blind source separation methods used for sEMG decomposition may produce duplicate MNDTs, with some MNDTs potentially identified twice across adjacent grids. Two MNDTs were considered duplicates if the agreement rate between two discharge trains exceeded 0.3, with the MNDT of the lower PNR removed (*22*). The decomposition parameters (separation matrix and spike extraction thresholds) obtained from the offline decomposition were used to decompose the sEMG signals in real time by directly multiplying the separation matrix by the sEMG signals. The discharges were extracted from the estimated MNDTs based on the preserved clustering centroids. The number and identity of MNDTs are defined during calibration. Although additional motoneurons may theoretically become active during subsequent contractions, this decomposition system does not attempt to detect new units but rather focuses on the reliable tracking of the calibrated units, prioritizing stability and computational efficiency in real-time applications.

Motoneuron clustering

The correlation between the smooth firing rates of motoneurons was calculated to assess the potential presence of common inputs among motoneurons (*51*). The MNDT was convolved with a 400-ms Hanning window to obtain the smooth firing rate of the motoneurons during the motor task. A 400-ms Hanning window was selected as it helps reduce the nonlinear effects between the input and output of motoneurons, resulting in an effective low-frequency neural drive at 2.5 Hz. The obtained firing rate was then passed through a 0.75 Hz high-pass filter to remove the DC component. Last, considering a time lag of −100 to +100 ms, the cross-correlation coefficient for each pair of motoneuron firing rates was calculated, resulting in a two-dimensional cross-correlation matrix.

Subsequently, the cross-correlation matrix, after applying a threshold of 0.7, served as an indicator of prominent correlation among the motoneurons. The performance of different correlation thresholds was evaluated using offline calibration across five healthy participants (table S5). The 0.7 threshold was ultimately selected because it yielded the highest peak correlations and fewer clusters. The 0-1 matrix (where 0 represents uncorrelated and 1 represents correlated) served as the adjacency matrix to construct a graph. The nodes represented motoneurons, and the edges connecting two nodes symbolized a significant correlation between them. Later, a multiresolution consensus clustering approach was applied to identify the clusters within the motoneuron network (*41*). As the first step in the consensus clustering, the number of partitions was set to 10,000 to cover the entire possible range of resolutions, from 1 cluster to n (the number of motoneurons) clusters. Second, the consensus matrix, which is defined as the number of partitions in which each pair of motoneurons belongs to the same cluster divided by the number of partitions in total, was computed, and the clustering method with the Genlouvain algorithm was applied to the consensus matrix the same times as the number of partitions in the first step (*41*). The second step would be repeated several times until a unique partition is reached.

Extraction of control commands

For each motoneuron cluster, the CST firing rate was extracted to represent the shared neural drive (*52*). The CST firing rate for each motoneuron cluster was then mapped to the activation level of each movement using a multivariate regression model

$$y_i = \sum_{m=1}^{n} a_m x_m + k \tag{4}$$

where y_i is the activation level of the ith movement calculated by averaging the absolute sEMG amplitudes across all channels in a sliding window during the ith segment, n is the number of motoneuron clusters, and a_m and k are constants trained via least squares fitting. The model was calibrated as follows: each participant performed the required movements sequentially, with each movement sustained for 20 s. The activation level y_i for the ith movement was calculated as the average absolute sEMG amplitude across all channels during the ith movement segment. As to segments of other movements, the activation level y_i was set to zero. The decomposed MNDTs were clustered into groups, and the CST feature from each cluster served as the input x_m to the model. CST and activation features were extracted with a window length of 300 ms and an overlap of 200 ms.

After calibration, the model was saved to the host computer. During the online test, the sEMG signals were processed, decomposed, and mapped to movement activation levels in real time. Neural features were extracted every 300 ms, with a 200 ms overlap between consecutive windows. When antagonistic movements were predicted, the model would output the movement with a higher activation level. The prosthesis is operated in speed control mode. The stronger the activation level of a participant's movement, the faster the prosthetics moved. In a relaxed state, the prosthesis does not return to a neutral position; instead, it maintains its current position. This mapping is instantaneous, with an update frequency of 10 Hz, generating a new output every 100 ms. To fine-tune the control speed of the prosthetics and minimize unintended activations, this study individually adjusted several parameters for each motion's activation: the activation threshold γ, the multiplication factor α, and the speed coefficient β. The final velocity command delivered to the ith DoF of the prosthesis was defined as

$$v_i = \begin{cases} 0 & \alpha_i y_i < \gamma_i \\ \beta_i \alpha_i y_i & \alpha_i y_i \geq \gamma_i \end{cases} \tag{5}$$

where the default values of y, α, and β were initialized as 0.1, 1, and 0.1, respectively. Among these, the activation threshold γ was fixed at 0.1 for all motions and not adjusted. α was typically between 0.5 and 2, and β between 0.05 and 0.3. Participants sequentially executed all motions while observing prosthetic responses. If a motion was continuously triggered during unrelated actions, its multiplication factor α_i was reduced in steps of 0.05 until unintended activations disappeared. Conversely, if a motion could not be performed even when the participant exerted maximum effort, α_i was increased in steps of 0.1 until the prosthesis could reliably execute the motion. This process was repeated iteratively until each motion could be executed stably and accurately. Typically, the tuning process for each motion required 1 to 2 adjustment cycles to achieve stable performance.

If the prosthetic response speed was satisfactory after this step, the speed coefficient β_i was left unchanged; otherwise, it was further tuned based on speed performance. Specifically, if a motion was difficult to perform smoothly at low speeds, β_i was decreased in steps of 0.05, whereas if the prosthesis failed to reach maximum speed, β_i was increased in steps of 0.05. This calibration procedure ensured that for each motion, the prosthesis could be reliably controlled to achieve both the minimum intended movement and the maximum available speed. These parameters are displayed in the graphical user interface, and the adjusted coefficients vary depending on the model and participant.

The control framework is similar to (*36*), but we optimized the electrode configuration, motion selection during calibration, position/velocity control modes, and scaling factors, to better adapt to amputees' requirements.

Comparison with conventional control

In this study, we selected the NMF-based, regression-based, and PR-based controllers as benchmark methods for comparison with our proposed approach. These controllers represent classical paradigms in myoelectric control that have been extensively validated in the literature (*1*, *26*, *42*). Their computational efficiency and robustness make them well-suited for real-time applications, and they remain among the most widely adopted strategies in current commercial prosthetic systems (*12*, *53*, *54*).

NMF-based control

The NMF-based control strategy models the root mean square (RMS) features of sEMG signals as a linear combination of basic components, as described in detail in (*42*). Mathematically, it represents the sEMG signal features as

$$X(t) = WF(t) \tag{6}$$

where $X(t)$ denotes the RMS features from all channels with dimensions $M \times T$, W is the synergy matrix with $M \times N$ dimensions, and $F(t)$ indicates the activation of synergies. Here, M is the number of sEMG channels, T represents the number of time steps in the training dataset, and N corresponds to the number of motions, which was set at 4 for 2-DoF tasks and 6 for 3-DoF tasks. The RMS features were extracted using a 300-ms sliding window, with a 200 ms overlap between consecutive windows, identical to the MNDT-based features, to ensure consistency. During training, the synergy matrix W was estimated iteratively using the standard multiplicative update rule for nonnegative NMF, which optimizes the approximation of $X(t)$ by minimizing the reconstruction error. In the prosthetic control experiments, the control signals for each movement were extracted using the pseudo-inverse matrix W^+ and the RMS features.

Regression-based control

Similar to the approach described in a previous study on dexterous upper-limb prosthetic control (*1*), the regression-based control strategy was based on MLR, which was modeled as

$$y_i = K\Phi \tag{7}$$

where y_i is the activation of ith motion calculated as in Eq. 4, Φ is the RMS feature in a sliding window, and K is the parameters estimated by the least-square method. The configuration of the sliding window was identical to that of the MNDT-based method. To ensure consistency across channels, the RMS features were normalized to the range of [0, 1] using min-max normalization. During online prediction, the same normalization parameters were applied to incoming features.

PR-based control

The PR-based control strategy classifies the RMS features of sEMG signals into different gestures with the linear discriminant analysis (LDA). The combination of RMS features with LDA achieves near-perfect classification accuracy when using high-density electrode arrays (*26*). The sliding window length for extracting RMS features was set to 300 ms, with a step size of 100 ms. For each 20-s movement segment, the central 15 s of data were extracted to form the RMS feature set, reducing edge effects. The original feature set was dimensionally reduced via principal component analysis, and the resulting principal components, which retained 99% of the explained variance, were used to form the calibration dataset. During the training phase, a hierarchical model was then used. In the first stage, LDA was trained on the calibration dataset to discriminate between different gesture classes. In the second stage, within each identified class, the RMS features were mapped to an activation level by applying min-max normalization parameters estimated from the calibration dataset, as shown in Eq. 4. In contrast to Eq. 4, activation here is computed exclusively within the temporal boundaries of each motion segment. These normalization parameters were saved and consistently applied during the online phase. In the prediction phase, the LDA provided class-level identification, while the class-specific normalization step transformed the corresponding RMS features into continuous activation levels, which were then used as control commands for the prosthesis.

To ensure a fair comparison, all methods were trained on identical datasets, using only the data from the calibration phase. The MNDT method used sEMG decomposition and neural drive extraction, whereas conventional controllers (NMF-based, regression-based, and PR-based) used the same preprocessed sEMG signals with their respective feature-extraction and modeling procedures.

Statistical analysis

For each experiment, the data analyzed consisted of the completion time of a single trial. We first performed a two-way ANOVA on completion times, with method (MNDT, NMF, MLR, and PR) and participant (S1 to S6) as factors. Considering intersubject differences, the model-based estimated means of completion times were calculated (tables S6 to S8). Similarly, to analyze the effect of arm position in experiment 2, a two-way ANOVA was conducted with participant and arm position (upper, middle, and lower) as factors, while the method factor was fixed. Each participant was further analyzed individually. The data were first tested for normality using the Kolmogorov-Smirnov test. Parametric tests were applied to normally distributed data. Otherwise, nonparametric alternatives were used. In experiment 1, either a one-way ANOVA or the Kruskal-Wallis test was performed separately for each participant to compare task completion times across the four methods (MNDT, NMF, MLR, and PR), based on the results of the normality test. The 3-DoF tasks in experiment 2 followed the same analysis procedure as those in experiment 1. For each participant, a one-way ANOVA or Kruskal-Wallis test was conducted to compare task completion times across the four methods, with five trials per method. In the 2-DoF task in experiment 2, each participant underwent two separate analyses. First, without considering arm position, a one-way ANOVA or Kruskal-Wallis test was performed to compare task completion times across the four methods, with 15 trials per method. Second, considering arm position, the results were grouped by the three arm positions (upper, middle, and lower). For each position, a one-way ANOVA or Kruskal-Wallis test was performed for each participant to compare the task completion times across the four methods (five trials per condition). For all statistical analyses, the significance level was set at 0.05.

Supplementary Materials

The PDF file includes:
Figs. S1 to S8
Tables S1 to S8
Legends for movies S1 to S5

Other Supplementary Material for this manuscript includes the following:
Movies S1 to S5

REFERENCES

1. J. M. Hahne, M. A. Schweisfurth, M. Koppe, D. Farina, Simultaneous control of multiple functions of bionic hand prostheses: Performance and robustness in end users. *Sci. Robot*. **3**, eaat3630 (2018).
2. D. Farina, R. Merletti, R. M. Enoka, The extraction of neural strategies from the surface EMG: 2004–2024. *J. Appl. Physiol.* **138**, 121–135 (2025).
3. A. Furui, S. Eto, K. Nakagaki, K. Shimada, G. Nakamura, A. Masuda, T. Chin, T. Tsuji, A myoelectric prosthetic hand with muscle synergy–based motion determination and impedance model–based biomimetic control. *Sci. Robot* **4**, eaaw6339 (2019).
4. T. A. Kuiken, L. A. Miller, K. Turner, L. J. Hargrove, A comparison of pattern recognition control and direct control of a multiple degree-of-freedom transradial prosthesis. *IEEE J. Transl. Eng. Health Med.* **4**, 2100508 (2016).
5. S. M. Sid'El Moctar, I. Rida, S. Boudaoud, Comprehensive review of feature extraction techniques for sEMG signal classification: From handcrafted features to deep learning approaches. *IRBM* **45**, 100866 (2024).
6. G. Gu, N. Zhang, H. Xu, S. Lin, Y. Yu, G. Chai, L. Ge, H. Yang, Q. Shao, X. Sheng, X. Zhu, X. Zhao, A soft neuroprosthetic hand providing simultaneous myoelectric control and tactile feedback. *Nat. Biomed. Eng.* **7**, 589–598 (2023).
7. J. He, X. Niu, P. Zhao, C. Lin, N. Jiang, From forearm to wrist: Deep learning for surface electromyography-based gesture recognition. *IEEE Trans. Neural Syst. Rehabil. Eng.* **32**, 102–111 (2024).
8. Z. Wei, Z.-Q. Zhang, S. Q. Xie, Continuous motion intention prediction using sEMG for upper-limb rehabilitation: A systematic review of model-based and model-free approaches. *IEEE Trans. Neural Syst. Rehabil. Eng.* **32**, 1487–1504 (2024).
9. E. Losanno, M. Mender, C. Chestek, S. Shokur, S. Micera, Neurotechnologies to restore hand functions. *Nat. Rev. Bioeng.* **1**, 390–407 (2023).
10. A. Holobar, D. Farina, Noninvasive neural interfacing with wearable muscle sensors: Combining convolutive blind source separation methods and deep learning techniques for neural decoding. *IEEE Signal Process. Mag.* **38**, 103–118 (2021).
11. C. J. Heckman, R. M. Enoka, Motor unit. *Compr. Physiol.* **2**, 2629–2682 (2012).
12. N. Jiang, C. Chen, J. He, J. Meng, L. Pan, S. Su, X. Zhu, Bio-robotics research for non-invasive myoelectric neural interfaces for upper-limb prosthetic control: A 10-year perspective review. *Natl. Sci. Rev.* **10**, nwad048 (2023).
13. T. Bao, S. Q. Xie, P. Yang, P. Zhou, Z.-Q. Zhang, Toward robust, adaptive and reliable upper-limb motion estimation using machine learning and deep learning–A survey in myoelectric control. *IEEE J. Biomed. Health Inform.* **26**, 3822–3835 (2022).
14. X. Li, Y. Liu, X. Zhou, Z. Yang, L. Tian, P. Fang, G. Li, Simultaneous hand/wrist motion recognition and continuous grasp force estimation based on nonlinear spectral sEMG features for transradial amputees. *Biomed. Signal Process. Control* **85**, 105044 (2023).
15. E. Eddy, E. Campbell, S. Bateman, E. Scheme, Understanding the influence of confounding factors in myoelectric control for discrete gesture recognition. *J. Neural Eng.* **21**, ad4915 (2024).
16. X. Wang, D. Ao, L. Li, Robust myoelectric pattern recognition methods for reducing users' calibration burden: Challenges and future. *Front. Bioeng. Biotechnol.* **12**, 1329209 (2024).
17. D. Farina, I. Vujaklija, M. Sartori, T. Kapelner, F. Negro, N. Jiang, K. Bergmeister, A. Andalib, J. Principe, O. C. Aszmann, Man/machine interface based on the discharge timings of spinal motor neurons after targeted muscle reinnervation. *Nat. Rev. Bioeng.* **1**, 0025 (2017).
18. D. Farina, D. F. Stegeman, R. Merletti, Biophysics of the Generation of EMG Signals, in *Surface Electromyography: Physiology, Engineering, and Applications* (2016), pp. 1–24.
19. M. Ortiz-Catalan, Neuroengineering: Deciphering neural drive. *Nat. Rev. Bioeng.* **1**, 0034 (2017).
20. D. Farina, I. Vujaklija, R. Brånemark, A. M. J. Bull, H. Dietl, B. Graimann, L. J. Hargrove, K.-P. Hoffmann, H. H. Huang, T. Ingvarsson, H. B. Janusson, K. Kristjánsson, T. Kuiken, S. Micera, T. Stieglitz, A. Sturma, D. Tyler, R. F. F. Weir, O. C. Aszmann, Toward higher-performance bionic limbs for wider clinical use. *Nat. Rev. Bioeng.* **7**, 473–485 (2023).
21. X. Zhang, G. Zhu, M. Chen, X. Chen, X. Chen, P. Zhou, Muscle force estimation based on neural drive information from individual motor units. *IEEE Trans. Neural Syst. Rehabil. Eng.* **28**, 3148–3157 (2020).
22. F. Negro, S. Muceli, A. M. Castronovo, A. Holobar, D. Farina, Multi-channel intramuscular and surface EMG decomposition by convolutive blind source separation. *J. Neural Eng.* **13**, 026027 (2016).

23. M. Chen, P. Zhou, 2CFastICA: A novel method for high density surface EMG decomposition based on kernel constrained fastICA and correlation constrained fastICA. *IEEE Trans. Neural Syst. Rehabil. Eng.* **32**, 2177–2186 (2024).
24. C. Chen, S. Ma, X. Sheng, D. Farina, X. Zhu, Adaptive real-time identification of motor unit discharges from non-stationary high-density surface electromyographic signals. *IEEE Trans. Biomed. Eng.* **67**, 3501–3509 (2020).
25. D. T. Michael, S. H. Roy, Z. Li, P. Contessa, G. De Luca, J. C. Kline, Motor unit drive: A neural interface for real-time upper limb prosthetic control. *J. Neural Eng.* **16**, 016012 (2019).
26. C. Chen, Y. Yu, X. Sheng, J. Meng, X. Zhu, Real-time hand gesture recognition by decoding motor unit discharges across multiple motor tasks from surface electromyography. *IEEE Trans. Biomed. Eng.* **70**, 2058–2068 (2023).
27. Y. Zheng, X. Hu, Real-time isometric finger extension force estimation based on motor unit discharge information. *J. Neural Eng.* **16**, 066006 (2019).
28. C. Chen, Y. Yu, X. Sheng, X. Zhu, Non-invasive analysis of motor unit activation during simultaneous and continuous wrist movements. *IEEE J. Biomed. Health Inform.* **26**, 2106–2115 (2022).
29. P. Capsi-Morales, D. Y. Barsakcioglu, M. G. Catalano, G. Grioli, A. Bicchi, D. Farina, Merging motoneuron and postural synergies in prosthetic hand design for natural bionic interfacing. *Sci. Robot.* **10**, eado9509 (2025).
30. T. Kapelner, M. Sartori, F. Negro, D. Farina, Neuro-musculoskeletal mapping for man-machine interfacing. *Sci. Rep.* **10**, 5834 (2020).
31. C. Dai, X. Hu, Finger joint angle estimation based on motoneuron discharge activities. *IEEE J. Biomed. Health Inform.* **24**, 760–767 (2020).
32. L. Meng, L. Varga, D. G. Kampe, X. Hu, Real-time myoelectric-based neural-drive decoding for concurrent and continuous control of robotic finger forces. *IEEE Trans. Hum. Mach. Syst.* **55**, 256–265 (2025).
33. C. Chen, Y. Yu, X. Sheng, J. Meng, X. Zhu, Mapping individual motor unit activity to continuous three-DoF wrist torques: Perspectives for myoelectric control. *IEEE Trans. Neural Syst. Rehabil. Eng.* **31**, 1807–1815 (2023).
34. Y. Yu, C. Chen, X. Sheng, X. Zhu, Wrist torque estimation via electromyographic motor unit decomposition and image reconstruction. *IEEE J. Biomed. Health Inform.* **25**, 2557–2566 (2021).
35. A. Holobar, D. Farina, Blind source identification from the multichannel surface electromyogram. *Physiol. Meas.* **35**, R143–R165 (2014).
36. R. Guo, C. Chen, X. Zhu, Simultaneous and proportional real-time control of three-DoF movements based on motor unit discharges. *IEEE J. Biomed. Health Inform.* **29**, 2642–2653 (2025).
37. Y. Xu, Y. Yu, Z. Zhao, X. Sheng, Decoding multi-DoF movements using a CST-based force generation model with single-DoF training. *IEEE Trans. Neural Syst. Rehabil. Eng.* **32**, 974–982 (2024).
38. T. Kapelner, F. Negro, O. C. Aszmann, D. Farina, Decoding motor unit activity from forearm muscles: Perspectives for myoelectric control. *IEEE Trans. Neural Syst. Rehabil. Eng.* **26**, 244–251 (2018).
39. C. Chen, S. Ma, Y. Yu, X. Sheng, X. Zhu, Segment-wise decomposition of surface electromyography to identify discharges across motor neuron populations. *IEEE Trans. Neural Syst. Rehabil. Eng.* **30**, 2012–2021 (2022).
40. A. Holobar, M. A. Minetto, D. Farina, Accurate identification of motor unit discharge patterns from high-density surface EMG and validation with a novel signal-based performance metric. *J. Neural Eng.* **11**, 016008 (2014).
41. L. G. S. Jeub, O. Sporns, S. Fortunato, Multiresolution consensus clustering in networks. *Sci. Rep.* **8**, 3259 (2018).
42. N. Jiang, H. Rehbaum, I. Vujaklija, B. Graimann, D. Farina, Intuitive, online, simultaneous, and proportional myoelectric control over two degrees-of-freedom in upper limb amputees. *IEEE Trans. Neural Syst. Rehabil. Eng.* **22**, 501–510 (2014).
43. M. Gherardini, V. Ianniciello, F. Masiero, F. Paggetti, D. D'Accolti, E. L. Frazia, O. Mani, S. Dalise, K. Dejanovic, N. Fragapane, L. Maggiani, E. Ipponi, M. Controzzi, M. Nicastro, C. Chisari, L. Andreani, C. Cipriani, Restoration of grasping in an upper limb amputee using the myokinetic prosthesis with implanted magnets. *Sci. Robot.* **9**, eadp3260 (2024).
44. A. M. Simon, K. Newkirk, L. A. Miller, K. L. Turner, K. Brenner, M. Stephens, L. J. Hargrove, Implications of EMG channel count: Enhancing pattern recognition online prosthetic testing. *Front. Rehabil. Sci.* **5**, 1345364 (2024).
45. C. Chen, Y. Yu, X. Sheng, D. Farina, X. Zhu, Simultaneous and proportional control of wrist and hand movements by decoding motor unit discharges in real time. *J. Neural Eng.* **18**, 056010 (2021).
46. Y. Zheng, X. Hu, Adaptive real-time decomposition of electromyogram during sustained muscle activation: A simulation study. *IEEE Trans. Biomed. Eng.* **69**, 645–653 (2022).
47. X. Shi, W. Guo, W. Xu, Z. Yang, X. Sheng, Semi-autonomous grasping control of prosthetic hand and wrist based on motion prior field. *IEEE Robot. Autom. Lett.* **9**, 5950–5957 (2024).
48. L. M. Hermansson, A. G. Fisher, B. Bernspång, A.-C. Eliasson, Assessment of capacity for myoelectric control: A new Rasch-built measure of prosthetic hand control. *J. Rehabil. Med.* **37**, 166–171 (2005).
49. L. Resnik, L. Adams, M. Borgia, J. Delikat, R. Disla, C. Ebner, L. S. Walters, Development and evaluation of the activities measure for upper limb amputees. *Arch. Phys. Med. Rehabil.* **94**, 488–494.e4 (2013).
50. A. Holobar, D. Zazula, *Gradient Convolution Kernel Compensation Applied to Surface Electromyograms* (Springer Berlin Heidelberg, 2007), pp. 617–624.
51. F. Hug, S. Avrillon, J. Ibáñez, D. Farina, Common synaptic input, synergies and size principle: Control of spinal motor neurons for movement generation. *J Physiol* **601**, 11–20 (2023).
52. A. Holobar, V. Glaser, Cumulative spike train outperforms the root-mean-square metric in muscle excitation estimation from dynamic high-density EMG, in *Converging Clinical and Engineering Research on Neurorehabilitation III. Biosystems & Biorobotics* (Springer, 2019), chap. 228, pp. 1143–1147.
53. E. Scheme, K. Englehart, Electromyogram pattern recognition for control of powered upper-limb prostheses: State of the art and challenges for clinical use. *J. Rehabil. Res. Dev.* **48**, 643 (2011).
54. L. J. Hargrove, L. A. Miller, K. Turner, T. A. Kuiken, Myoelectric pattern recognition outperforms direct control for transhumeral amputees with targeted muscle reinnervation: A randomized clinical trial. *Sci. Rep.* **7**, 13840 (2017).

Acknowledgments

Funding: This work was supported by the National Natural Science Foundation of China (52227808, X.Z.), National Natural Science Foundation of China (52575030 and 52205024, C.C.), National Natural Science Foundation of China (52375021, W.G.), and Shanghai Jiao Tong University (SD6040004/110 and WH220502012, C.C.). **Author contributions:** Conceptualization: C.C., R.G., X.Z., and G.G. Methodology: R.G., C.C., D.L., S.S., and W.G. Software: R.G. and D.L. Validation: C.C., R.G., and D.L. Formal analysis: C.C., R.G., and D.L. Investigation: C.C., R.G., D.L., S.S., J.M., and W.G. Resources: C.C., R.G., D.L., W.G., J.M., G.G., and X.Z. Data curation: C.C., R.G., and D.L. Writing–original draft: C.C., R.G., and D.L. Writing–review and editing: C.C., R.G., D.L., G.G., X.Z., S.S., J.M., and W.G. Visualization: C.C., R.G., D.L., and G.G. Supervision: X.Z., G.G., and J.M. Project administration: X.Z., C.C., and G.G. Funding acquisition: X.Z., C.C., and W.G. **Competing interests:** The authors declare that they have no competing interests. **Data, code, and materials availability:** All data and code needed to evaluate and reproduce the results in the paper are present in the paper, the Supplementary Materials, and Zenodo at https://doi.org/10.5281/zenodo.20676181. This study did not generate new materials.

Submitted 20 May 2026
Accepted 23 June 2026
Published 31 July 2026
10.1126/sciadv.aej0245

Science Advances

A motoneuron discharge–driven interface realizing simultaneous and proportional control of prosthetics in end-users

Chen Chen, Ruye Guo, Dongxuan Li, Shang Shi, Weichao Guo, Jianjun Meng, Guoying Gu, and Xiangyang Zhu

Sci. Adv. **12** (31), eaej0245. DOI: 10.1126/sciadv.aej0245